Shock formation in flowing plasmas by temporally and spatially smoothed laser beams

J D Ludwig, S Hüller, H A Rose, C Bruulsema, W Farmer, P Michel, A Milder, G F Swadling, W Rozmus

Shock formation in flowing plasmas by temporally and spatially smoothed laser beams

J. D. Ludwig,[1] S. Hüller,[2] H. A. Rose,[3] C. Bruulsema,[1] W. Farmer,[1] P. Michel,[1] A. Milder,[4] G. F. Swadling,[1] and W. Rozmus[4]

[1)] *Lawrence Livermore National Laboratory, 7000 East Avenue, Livermore, California 94551, USA*

[2)] *Centre de Physique Théorique CPHT, CNRS, Ecole polytechnique, Insitut Polytechnique Paris, 91128 Palaiseau Cedex, France*

[3)] *Los Alamos National Laboratory, Los Alamos, New Mexico, USA 87545*

[4)] *Department of Physics, University of Alberta, Edmonton, Alberta, Canada T6G 2E1*

(Dated: 24 October 2023)

The cumulative impact of multiple laser speckles on the supersonic plasma flow across optically smoothed laser beams is investigated. The bending of the laser beams caused by ponderomotive laser-plasma coupling, together with flow, lead to plasma response by momentum conservation that results in a deceleration of the flow. Once the flow velocity decreases to a subsonic level, the action of the laser beams can generate a shock within the plasma. This scenario has been predicted theoretically and confirmed by hydrodynamic simulations. The conditions of shock generation are given in terms of the ponderomotive pressure, speckle size and the flow velocity. The nonlinear properties of the shocks are analyzed using Rankine-Hugoniot relations. According to linear theory, temporally smoothed beams exhibit a higher threshold for shock generation. Numerical simulations with beams that are smoothed by spectral dispersion compare well with the linear theory results, diverging from those produced by beams with only a random phase plates in the nonlinear regime. The conditions necessary for shock generation and their effects on the laser plasma coupling in the inertial confinement fusion experiments are also discussed.

Keywords: Laser Shock, beam bending, laser plasma interaction of optically smoothing laser beams

I. INTRODUCTION

Inertial Confinement Fusion (ICF) faces challenges with implosion symmetry, energy coupling and variety of laser plasma-interaction (LPI) processes that become experimentally accessible and relevant for the performance of the ICF targets. For example, implosion symmetry is known to be strongly affected by Cross Beam Energy Transfer (CBET). Energy transfer between laser beams occurs when an ion acoustic wave is in resonance with the ponderomotive force due to overlapping laser beams. In the case of beams with equal frequency intersecting each other, plasma flow at the ion sound speed and the Doppler shift of the ion acoustic frequency can establish this resonance[1–7]. In a flowing plasma, the process of beam bending in the direction of the flow velocity has been examined in theory and experiments[8–11]. The skewed by flow density perturbations due to the ponderomotive force of the light redirect laser beams and by momentum conservation introduce a drag on the plasma flow slowing it down. The rate of beam bending is maximized when the plasma flow is at the sound speed, resulting in the largest drag and flow deceleration. As the flow transitions from supersonic to subsonic velocity, conditions conducive to shock generation in a plasma are formed. Such shocks and related density and velocity perturbations have not been examined so far and are the main focus of our work.

While a shock can be generated by a coherent laser beam, much smaller beam intensity and energy are required for shock formation in spatially randomized beams, as produced by the use of a random phase plate (RPP). This effect is attributed to the stronger ponderomotive force exerted on the plasma by the small-scale speckles generated in such beams. Even though local flow perturbations on the scale of individual speckles may be minimal, their cumulative effect, especially when the flow interacts with large-scale ICF beams, will lead to shock formation[12–14]. Furthermore, shock generation can be intensified in the region where beams intersect. Crossing beams results in a reduction in the effective size of the speckles. This reduction amplifies the ponderomotive force on the flow, which is further augmented by the increased laser intensity due to beam overlap. In ICF experiments, temporal smoothing techniques like smoothing by spectral dispersion (SSD) are applied to large-scale laser beams. Our investigation into the effects of SSD on shock generation, through linear theory calculations, has revealed an enhancement of threshold conditions and an increase in the required penetration length of the plasma flow across the laser beam.

The shocks discussed in our article originate gradually within the plasma as it traverses a randomized laser beam. Upon separation from the laser, it takes on the form of a bow shock enveloping the whole beam. This shock induces perturbations in both density and flow velocity, extending beyond the laser and potentially influencing LPI processes across a sizable portion of the target. The underlying physical mechanisms for shock formation are common in ICF experiments. However, detecting freely propagating shocks in experiments may necessitate specific experimental configurations and precise plasma parameters. For instance, our theoretical model of an isothermal plasma, displays a relatively slow velocity of nonlinear shock propagation, thereby amplifying the energy requirements for the laser beam by increasing its required time duration. This limitation may hamper observation of the ponderomotively driven shock, restricting it to conditions akin to

those at the National Ignition Facility (NIF), requiring tens of kilojoules of energy per beam. In the ongoing campaigns on the less powerful OMEGA laser we have demonstrated shock generation due to thermal enhancements of the ponderomotive laser plasma coupling and will report on results of experiments in the subsequent publication[15].

The rest of this article is organized as follows: in sections II and III we present the theoretical basis for beam deflection and its action on the plasma flow. In section IV, results from numerical simulations are presented and analyzed. Section V concludes the article with a discussion of implications for ICF experiments.

II. TRANSVERSE PLASMA FLOW AND BEAM DEFLECTION

In a collisionless laser-produced plasma, the equations of the fluid model for density and momentum conservation in the limit of low-frequency plasma response for cold ions,

$$\frac{\partial n_i}{\partial t}+\nabla\cdot(n_i\vec{v}_i)=0\,,\quad \frac{\partial \vec{v}_i}{\partial t}+(\vec{v}_i\cdot\nabla)\vec{v}_i=-\frac{Ze}{m_i}\nabla\phi, \tag{1}$$

can be simplified by assuming the case of an isothermal plasma[16–18], such that the electrostatic potential ϕ together with the ponderomotive potential U of the laser quiver motion relate to the electron density n_e via the Boltzmann factor

$$n_e=n_0\exp(e\phi/T_e-U/T_e)\,, \tag{2}$$

with T_e denoting the electron temperature.

The ponderomotive potential U is defined in terms of the laser electric field $\vec{\mathscr{E}}=\frac{1}{2}[\vec{E}e^{-i\omega_0 t}+c.c.]$ with its amplitude $\vec{E}$ as

$$U=e^2|\vec{E}|^2/(4m_e\omega_0^2); \tag{3}$$

the electromagnetic field amplitude $\vec{E}$ satisfies the time enveloped wave equation,

$$2i\frac{\partial\vec{E}}{\partial t}+(c^2/\omega_0)\nabla^2\vec{E}+\omega_0(1-n_e/n_c)\vec{E}=0. \tag{4}$$

When transverse fluctuations in a laser field are large compared to fluctuations along the propagation axis, the hydrodynamic model may be simplified to two dimensions, so that only the fluid momentum component perpendicular to the laser axis is effected. The direction of the propagation of a laser is along the z-axis and the flow velocity will be in the x - y plane (cf. Fig. 1).

By denoting $\vec{p}_\perp=\rho\vec{v}_\perp$ as the plasma fluid momentum density in the direction perpendicular to the laser propagation and $c_s=(ZT_e/m_i)^{1/2}$ as the sound speed, with $\rho\equiv n_e/n_0$ the isothermal fluid equations (1) with Eq. (2) read,

$$\frac{\partial\vec{p}_\perp}{\partial t}+\nabla_\perp\cdot(\vec{v}_\perp\vec{p}_\perp)=-c_s^2\rho\nabla_\perp\left(\ln\rho+\tfrac{U}{T_e}\right)\,, \tag{5}$$

$$\frac{\partial\rho}{\partial t}+\nabla_\perp\cdot\vec{p}_\perp=0\,. \tag{6}$$

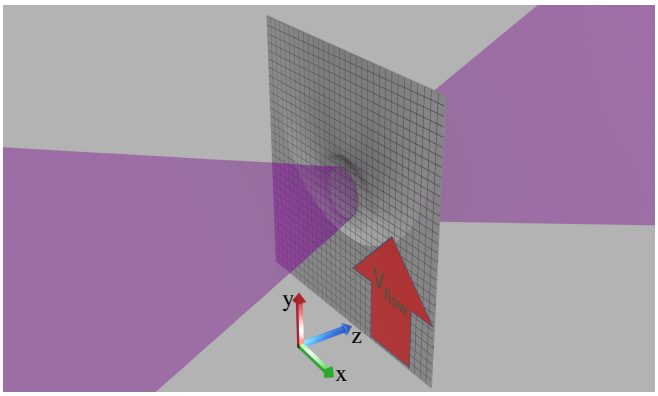

FIG. 1. Sketch of the geometry in numerical simulations: the laser is passing through the plasma located around the focal region. This is represented in the simulations by a two-dimensional (2D) domain (area shaded in gray) in the plane of the laser beam cross section at best focus. The plasma flow is in the vertical direction (arrow) within the simulation plane and perpendicular to the laser propagation direction.

In absence of flow, a stationary equilibrium can be reached via the balance between of the local density and the ponderomotive potential, namely $\rho_0=(n_e/n_0)_{v_\perp=0}\equiv\exp(-U/T_e)$. It has, however, been shown that flow can considerably modify the response of the plasma fluid[9,19–22].

To obtain analytical results it is useful to consider in the fluid equations (5),(6) a small velocity perturbation and to linearize the momentum equation about background flow velocity, $\vec{v}_0$ in the x - y plane, $\vec{v}_\perp=\vec{v}_0+\delta\vec{v}_\perp$. This leads to the following set of equations[9]

$$\left(\tfrac{\partial}{\partial t}+\vec{v}_0\cdot\nabla_\perp\right)\ln\rho+\nabla_\perp\cdot\delta\vec{v}_\perp=0, \tag{7}$$

$$\left(\tfrac{\partial}{\partial t}+\vec{v}_0\cdot\nabla_\perp\right)\delta\vec{v}_\perp+2\nu_{ia}\delta\vec{v}_\perp=-c_s^2\nabla_\perp\left(\ln\rho+\tfrac{U}{T_e}\right) \tag{8}$$

where ν_{ia} is a spatial convolution operator approximating Landau damping of ion acoustic perturbations. The time independent solution of Eqs. (7), (8) in Fourier space reads[9]

$$(\ln\rho)_{k_\perp}=\frac{(\ln\rho_0)_{k_\perp}}{1-(k_y/k_\perp)M(k_yM/k_\perp-2i\hat{\nu})}\,, \tag{9}$$

where the background flow $\vec{v}_0$ is chosen along the y-axis, the Mach number $M=v_0/c_s$ and the normalized damping operator $\hat{\nu}=\nu_{ia}/(kc_s)$. The density perturbation Eq. (9) displays a skewed profile due to the flow compared to ρ_0 in the stationary plasma and the ponderomotive potential U of a single laser speckle. This asymmetry in density perturbations averaged over speckles of the randomized laser beam leads to beam bending. In the small angle approximation the beam bending can be quantified by the average angular deflection rate[9]

$$\frac{\partial\langle\theta\rangle}{\partial z}=\frac{\partial}{\partial z}\left\langle\frac{\vec{k}_\perp}{k_0}\right\rangle_k\cdot\frac{\vec{v}_0}{|\vec{v}_0|}=-\frac{1}{2}\frac{n_0}{n_c}\left\langle\nabla_\perp\frac{\delta n}{n_0}\right\rangle_r\cdot\frac{\vec{v}_0}{|\vec{v}_0|}\,, \tag{10}$$

where the small density perturbation $\delta n/n_0=\rho-1$ or alternatively $\ln\rho\approx\delta n/n_0$. The average in the two dimensional

k-space of any function $h(\vec{k}_\perp)$ is calculated according to the following expression

$$\langle h\rangle_k(z) = \frac{\int d^2k_\perp |E(\vec{k}_\perp,z)|^2 h(\vec{k}_\perp)}{\int d^2k_\perp |E(\vec{k}_\perp,z)|^2} \tag{11}$$

while the spatial average of any function $g(\vec{r}_\perp)$ reads

$$\langle g\rangle_r(z) = \frac{\int d^2r_\perp |E(\vec{r}_\perp,z)|^2 g(\vec{r}_\perp)}{\int d^2r_\perp |E(\vec{r}_\perp,z)|^2} \tag{12}$$

The rate of beam deflection Eq. (10) and the averaging defined in Eqs. (11), (12) involve the electric field amplitude $\vec{E}$ obtained from the wave equation (4) in the paraxial approximation.

III. DRAG ON PLASMA FLOW DUE TO BEAM DEFLECTION

Analytical results in this Section are derived using an expression for the beam deflection rate, Eq.(10). Furthermore we use the results from section V.A of Ref. 13, in particular Eq. (157), which was derived for the ponderomotive potential assuming a stationary, random-valued field pattern with weak amplitude representing a beam generated by a random phase plate (RPP). Equation (10) yields then the following expression for $M > 1$

$$\frac{\partial}{\partial z}\left\langle \frac{\vec{k}_\perp}{k_0}\right\rangle_k \cdot \frac{\vec{v}_0}{|\vec{v}_0|} = \frac{2}{\ell_{\rm RPP}}\frac{\langle n\rangle}{n_c}\frac{\langle U\rangle}{T_e} f(M,\hat{v}), \tag{13}$$

where the brackets $\langle\rangle_k$, Eq. (11) indicate an average over a speckle ensemble, $\ell_{\rm RPP} = \frac{45}{64}F\lambda$ denotes the speckle correlation length of an RPP beam[13], and n_c the critical density. Similar expressions in the context of beam bending[11,21,22] have been derived, with the dependence on the plasma density n, the average ponderomotive potential $\langle U\rangle$, and the speckle (or beam) width $\sim F\lambda$, with F denoting the beam optics F-number. Note that the averaged plasma density $\langle n\rangle$ and the average ponderomotive potential $\langle U\rangle/T_e$ normalized to the electron temperature can be assumed to vary slowly on the speckle's width $F\lambda$ and response time $F\lambda/c_s$. The ponderomotive potential in the above expression is related to the density fluctuations for the case of a stationary plasma, namely $(\delta n/\langle n\rangle)_{v_\perp=0} = 1-\rho_0 \approx U/T_e$.

Following Ref. 13, the function $f(M,\nu_{ia})$ is given by:

$$f(M,\nu_{ia}) = \frac{2}{\pi}\int_0^{\pi/2} \frac{M\nu_{ia}\cos^2\theta}{(1-M^2\cos^2\theta)^2+4M^2\nu_{ia}^2\cos^2\theta}d\theta\ , \tag{14}$$

where ν_{ia} is the ion acoustic damping rate normalized to the ion acoustic frequency and $\vec{k}_\perp\cdot\vec{v}_0 = |\vec{k}_\perp||\vec{v}_0|\cos\theta$. The integral represents a uniform disk of transverse wavenumber Fourier amplitudes with radius $\pi/F\lambda$.

The case of the $M=1$ singularity and its vicinity is integrable, so that if M varies with z and goes through a sonic point the total angular deflection is finite.

In the limit of small damping $\nu_{ia}\to 0$ for supersonic flow, $M>1$, the function $f(M,\nu_{ia})$ can be approximated by:

$$\lim_{\nu_{ia}\to 0} f(M,\nu_{ia}) \approx \tilde{f}(M) \equiv \frac{1}{2M\sqrt{M^2-1}}, \tag{15}$$

The cumulative action of the ponderomotive force from numerous speckles can be evaluated by separating the mean values and the fluctuation of the fluid quantities, namely $\rho = \langle\rho\rangle + \delta\rho$ and $\vec{p}_\perp = \langle\vec{p}_\perp\rangle + \delta\vec{p}_\perp$, in Eqs. (5) and (6). Following Refs. 9 and 23, the loss in fluid momentum as a function of time due to the collective action of speckles can be derived by ignoring the averages of fluctuating terms except in the last term on the RHS of Eq. (5). The fluctuation coupling results in equations for the averages $\langle\vec{p}_\perp\rangle$ and $\langle\rho\rangle$,

$$\frac{\partial\langle\vec{p}_\perp\rangle}{\partial t} + \nabla_\perp\cdot(\langle\vec{p}_\perp\rangle\langle\vec{v}_\perp\rangle) = -\alpha\langle\vec{p}_\perp\rangle - c_s^2\langle\rho\rangle\nabla_\perp\left(\ln\langle\rho\rangle + \frac{\langle U\rangle}{T_e}\right) \tag{16}$$

$$\frac{\partial\langle\rho\rangle}{\partial t} + \nabla_\perp\cdot(\langle\rho\rangle\langle\vec{v}_\perp\rangle) = 0, \tag{17}$$

with a drag (source) term $-\alpha\ \langle\vec{p}_\perp\rangle$. When $\langle U\rangle/T_e$ is small, the drag term, $\alpha\ \langle\vec{p_\perp}\rangle$, points along the local momentum direction for the isotropic RPP disk model such that α is simply a coefficient. Otherwise, α must be generalized to a tensor. The drag coefficient, α, as given by Eq. (28) of Ref. 9, reads

$$\alpha = 2\frac{\langle U\rangle}{T_e}\frac{n_c}{\langle n\rangle}\frac{c_s}{M}\frac{\partial\langle\theta\rangle}{\partial z} = \frac{4\,c_s}{\ell_{\rm RPP}}\left(\frac{\langle U\rangle}{T_e}\right)^2\frac{f(M,\nu_{ia})}{M}. \tag{18}$$

We can now find analytic results for shock formation due to drag from an idealized laser beam whose spatial envelope is a slab, only varying in the y-direction for incident flow with Mach number $M>1$, specified at $y=0$, with an initial unperturbed density profile. The combined effect of laser speckles, as described by the drag coefficient, leads to the deceleration of supersonic flow, transitioning it from supersonic to subsonic velocities, which in turn signifies the occurrence of shock formation. From Eqs. (13-15,16-18), assuming steady state flow in the positive y-direction,

$$\langle\rho\rangle\left(\frac{(\langle\vec{v}_\perp\rangle\cdot\nabla_\perp)\langle\vec{v}_\perp\rangle}{c_s^2} + \frac{\nabla_\perp\langle\rho\rangle}{\langle\rho\rangle} + \frac{\alpha}{c_s}\frac{\langle\vec{v}_\perp\rangle}{c_s}\right) = -\langle\rho\rangle\nabla_\perp\frac{\langle U\rangle}{T_e} \tag{19}$$

together with $\langle\rho\rangle\langle v_\perp\rangle \equiv \langle\rho\rangle M c_s$ and $\nabla_\perp\to\partial_y$, neglecting for simplicity the right-hand-side term in Eq. (19) one obtains

$$\frac{d}{dy}\left(M+\frac{1}{M}\right) = -\frac{\alpha}{c_s}\ . \tag{20}$$

Then, using the small damping limit Eq. (15) in Eq. (18) for α, the steady state solutions of Eqs. (16) and (17) imply

$$\frac{d}{dy}\left(M+\frac{1}{M}\right) = -\frac{2}{\ell_{\rm RPP}}\left(\frac{\langle U\rangle}{T_e}\right)^2\frac{1}{M^2\sqrt{M^2-1}}\quad . \tag{21}$$

Sonic flow, $M=1$ is reached at $y=y_{\rm sonic}$

$$y_{sonic} = \frac{\ell_{\rm RPP}}{2}\left(\frac{\langle U\rangle}{T_e}\right)^{-2}\int_1^M (u^2-1)^{3/2}du \tag{22}$$
$$= \frac{45}{1024}y_p\left(M(2M^2-5)\sqrt{M^2-1} + 3\ln\left[2(\sqrt{M^2-1}+M)\right]\right),$$

wherein $y_p = F\lambda/(\frac{\langle U\rangle}{T_e})^2$ is the scaling length. Figure 2 shows $y_{\rm sonic}$, Eq. (22) in comparison to results of numerical solutions of the fluid equations (5), (6). Details of simulations and nonlinear limit of shock formation are discussed next in section IV.

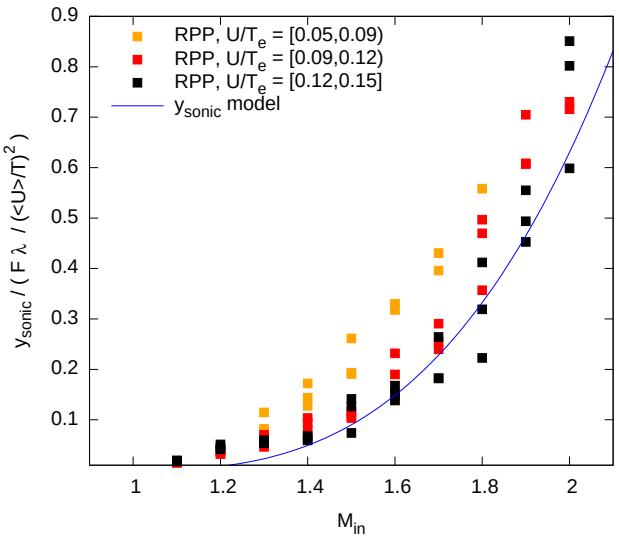

FIG. 2. Position of the point along the y-axis at which sonic flow is reached, y_{sonic}, as a function of the incoming flow Mach number M_{in}. The solid line shows the y_{sonic} position according to Eq. (22). Data points correspond to hydrodynamic simulations[24,25] including ponderomotive action of the laser beam speckle pattern of a beam generated with RPP. Parameters: n/n_c =0.1, $F = 8$. The $y_{\rm sonic}$ axis is scaled to $y_p = F\lambda/(\langle U\rangle/T_e)^2$. The colour of the data points indicates the range of the average ponderomotive potential, orange for $0.05 \leq \langle U\rangle/T_e < 0.09$, red for $0.09 \leq \langle U\rangle/T_e < 0.12$, and black for $0.12 \leq \langle U\rangle/T_e < 0.15$.

IV. NUMERICAL SIMULATIONS AND NONLINEAR SHOCKS

Numerical solutions of Eqns. (5), (6) in the plane normal to the beam propagation (see Fig. 1) have been computed using a two-dimensional (2D) isothermal variant of the Clawpack package, initially developed by LeVecque et al.[26]. This code has been further enhanced in Ref. 25 by incorporating a ponderomotive force term into the momentum equation. The majority of the simulations have been carried out for an electron density of n_e =0.1n_c, with n_c denoting the critical density, and for the laser F-number F =8. The spatial domain was resolved with 4096x4096 mesh points. The simulations were performed in dimensionless units. Taking a laser wave length of λ =0.351μm this corresponds to a spatial resolution of $dx = dy$ =0.4826μm for a domain size with $L_x = L_y$ =1.9768mm. Times are given, in the following, in ps by assuming ZT_e/A = 1keV for the evaluation of the sound speed in the conversion with λ/c_s.

A. Random phase plate beams

In the RPP top hat model of intensity distribution each Fourier mode of the laser light electric field $\vec{E}$ within the x-y plane of the plasma flow is assigned a random phase $\phi(\vec{k})$ and the constant amplitude $|E(\vec{k})|$ for $|\vec{k}| \leq k_0/(2F)$ where k_0 is the laser wavenumber. The speckle patterns produced by such disk-shaped RPP beams are evident in Fig. 3 in the density and flow velocity perturbations.

The space-time evolution of the plasma flow and the gradual shock formation leading to a free shock propagation against plasma flow with a well defined velocity is illustrated in Fig. 4. The values of density and velocity in Fig. 4 are extracted from two-dimensional density and velocity fields $\rho(x,y)$,$v_y(x,y)$ at the central position in x with respect to the speckle pattern (here $x \simeq 1000\mu m$) along y.

In the early stage of the shock formation, a position at y_{sonic} along the y-axis can be identified by the location of the earliest transition from the supersonic ($y < y_{sonic}$) to subsonic flow velocities ($y > y_{sonic}$). For our simulations, all carried out for ponderomotive potential values $\langle U\rangle/T_e > 0.015$, this usually occurs in the vicinity of the earliest intense laser speckle situated close to the edge of the laser beam envelope. Behind this position (in the flow direction, here y) the flow may again exceed c_s before the next, i.e. a neighbouring and/or subsequent intense speckle slows the incoming flow. The transition from super-sonic to sub-sonic may be repeated several times along the flow direction. It is then the combined action of the speckle ensemble that eventually leads to a shock formation.

We have determined positions y_{sonic} for a set of simulations by varying the incoming flow Mach numbers M_{in} and the average ponderomotive potential associated with the smoothed beam. These results are shown in Fig. 2 and are compared to the expression given by Eq. (22), taking into account a correction[27] with respect to the simulations due to the gradual rise in the envelope of the average laser intensity value in the wings of the laser beam envelope for a width of 70μm (i.e. $\sim 200\lambda$). The comparison shows good agreement between simulations and the model developed in section III. For the early stage, only the ponderomotively imprinted perturbations in the flow and the density are seen, as illustrated in both sublplots in Fig. 3, left column.

Later on, as shown in the right column subplots of Fig. 3, at $t = 2377$ps, a clean bow shock front propagates against the flow coming from below, here with $M_{in} = 1.1$.

Figure 4 shows that this clear and sharp shock front occurs, here beyond $t \simeq 1100$ps, once the collectively formed perturbation leaves the zone of influence of the laser beam speckle pattern. Behind this front, the flow remains then sub-sonic, except close to intense speckles further inside the beam. Figure 3, for a late time, here $t = 2377ps$, displays a sharp shock front propagating down against the background plasma flow of $M_{in} = 1.1$. Figure 5 illustrates, correspondingly, the profiles for density (red curve) and flow (blue) as a function of y taken from a simulation in the central cut of the laser beam, i.e. $x \simeq 1000\mu$m in Fig. 3, showing clear jumps left of the spatial zone occupied by the laser beam $750 < y(\mu m) < 1350$.

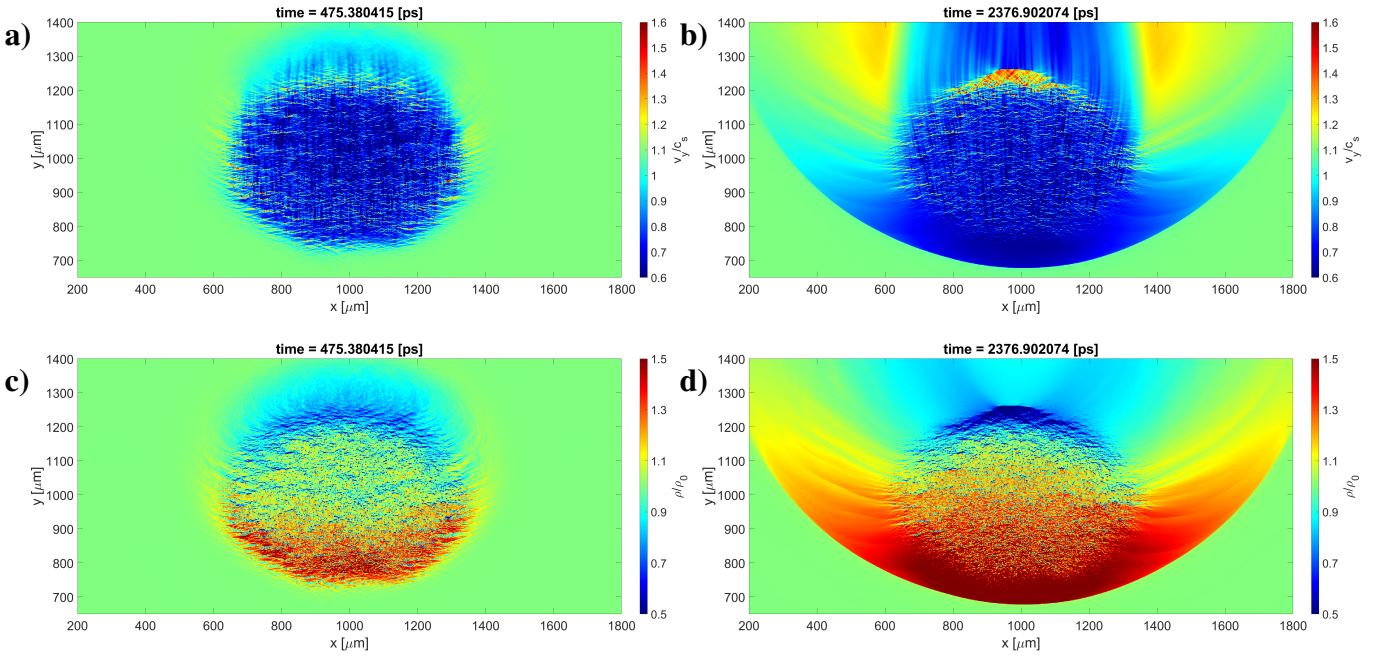

FIG. 3. Plasma flow v_y/c_s (top, a, b) and density n/n_0 (bottom c,d) cross sections in x and y at early time (left, a,c) and late time (right, b,d) of a simulation with incoming flow at M_{in} =1.1 (from below) and an average normalized laser ponderomotive potential $\langle U\rangle/T_e = 0.13$. The early images (left) show the imprint of the laser beam cross section with speckle structure while the late images (right) show a developed shock with a clear front departing from the laser speckle pattern.

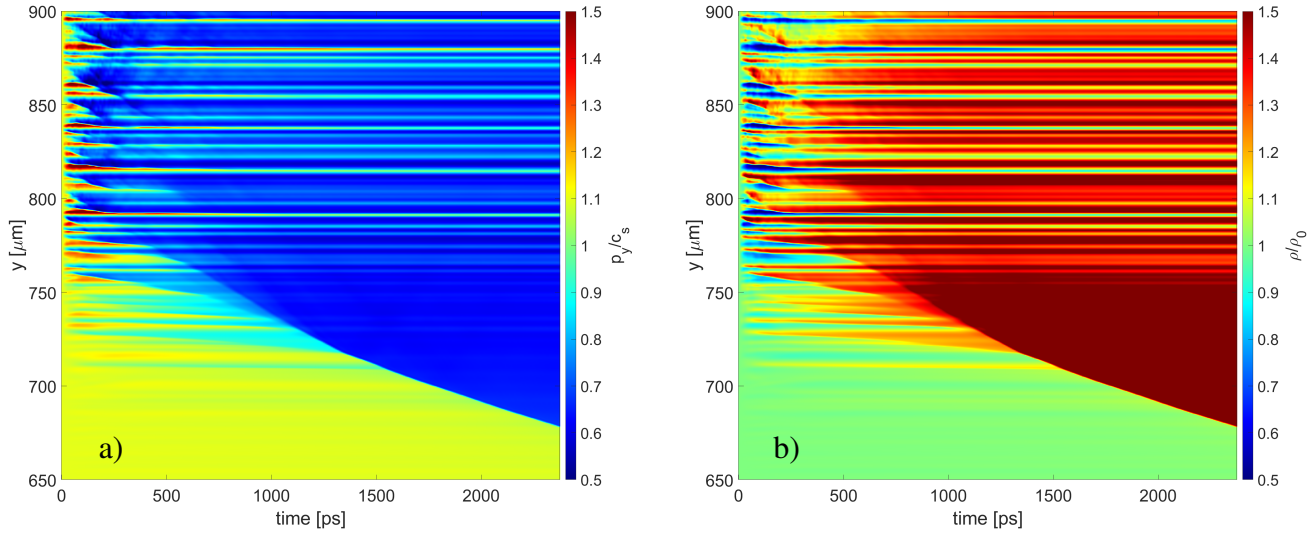

FIG. 4. Plasma flow velocity v_y/c_s (left, a) and plasma density (right, b) as a function of time on the horizontal axis from a line-out in y through the center of the simulation box at x=1000μm. The image corresponds to the same simulation as in Fig. 3 with M_{in} =1.1 and $\langle U\rangle/T_e = 0.13$. Note the sharp transition occurs (in both the flow and density) and moves out of the speckle pattern at a nearly constant speed during late times (t >1300ps). The position in y of the transition from super- to sub-sonic flow is, for this case, around $y_{sonic} = y \simeq 715\mu m$. The slope of this line is used to determine the shock speeds later on shown in Figure 7.

B. Density and momentum jumps due to shocks

For series of simulations with three different values of the incoming super-sonic flow, namely M_{in} =1.05, 1.1, 1.2, and 1.3, we have determined the jumps in density as a function of the ponderomotive potential $\langle U\rangle$. The results shown in Fig. 6 correspond to the cases of optically smoothed laser beams using (i) the method with random phase plates, RPP, without temporal incoherence and (ii) the spatio-temporal smoothing method 'Smoothing by Spectral Dispersion', SSD. The resul-

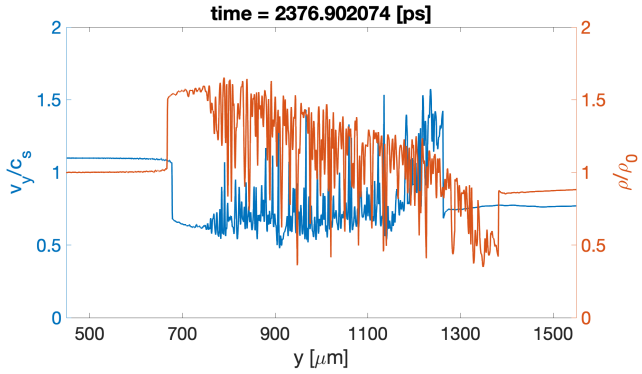

FIG. 5. Plasma density n/n_0 (red line) and flow v_y/c_s (blue) as a function y taken from a line-out the center of the simulation box at x=1000μm at $t = 2376$ps. The image corresponds to the same simulation as in Figs. 3- 4 with M_{in} =1.1 and $\langle U\rangle/T_e = 0.13$, and to the latest line-out in time of Figs. 4. Both quantities show a shock front running against the incoming flow, located around y =700μm, well outside the beam.

ing density jumps increase with the ponderomotive drive, and are stronger for higher incoming flow. It results that the ratio between the density jumps for the same $\langle U\rangle$ value are almost linearly proportional to M_{in}. We have examined whether the

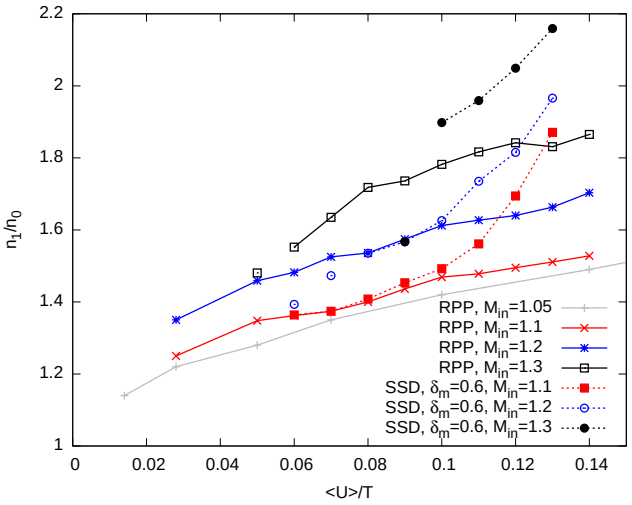

FIG. 6. Density jump, n_1/n_0 over the shock as a function of the average value of the ponderomotive potential $\langle U\rangle/T_e$ are displayed for both RPP cases (solid lines) and for selected SSD cases (dashed) with phase depth , δ_m =0.6. The lines correspond to different values of the incoming flow, M_{in} =1.05 (only RPP), 1.1, 1.2, and 1.3.

observed jumps in density and flow velocity fulfill the conditions expected for a shock, namely whether – once far away from the influence of the beam – they fulfill the Rankine-Hugoniot relations resulting from continuity, momentum, and energy balance in the frame of the shock, the details of which are discussed in the Appendix. These relations eventually reveal the jumps in density and flow velocity between both sides of the shock. We denote with n_0 the plasma density in front of the shock, in the unperturbed plasma, and n_1 the plasma density behind the shock, usually assuming $n_1 > n_0$. Likewise we define the plasma flows $v_{y,0}$ and $v_{y,1}$, in the laboratory frame. $M_{in} = v_{y,0}/c_{s,0}$ is the Mach number of the incoming flow; $c_{s,j}$ denotes the sound speed in front (j =0) and behind (j =1) the shock front, respectively. The Mach numbers in the Rankine-Hugoniot relations are those of the shock frame which can be determined from $v_{y,0}/c_{s,0}$ and $v_{y,1}/c_{s,1}$ via the shock speed in the laboratory frame v_{sh}, readily given by given by $M_0 = (v_{y,0} - v_{sh})/c_{s,0}$ and $M_1 = (v_{y,1} - v_{sh})/c_{s,1}$.

For the current study we have considered the case of an isothermal plasma (with $\gamma = 1$, degrees of freedom $\to \infty$), being a particular case, for which the relation between the internal energies on both sides of the jump, see Eq. (A.3), can be disregarded. For the isothermal plasma case with $c_{s,0} = c_{s,1} \equiv c_s$, the set of Rankine-Hugoniot relations is simplified to the continuity and Euler equations (see Eqs. (A.6)-(A.7)), such that the resulting density jump is then essentially a function of the Mach numbers, $n_1/n_0 = M_0^2 = M_1^{-2}$ together with $M_0 M_1 = 1$.

From our simulations the shock speed in the laboratory frame, v_{sh}, has been deduced from the space-time slope of the shock front, an example of which is illustrated in Fig. 4. One can consequently determine the Mach numbers M_0 and M_1 on each side of the shock, and n_1, while n_0 and M_{in} are known from the unperturbed plasma. For the case of an isothermal plasma it follows from Eq. (A.8), $-v_{sh}/c_s = \sqrt{n_1/n_0} - M_{in}$, that the formation of a shock propagating against the incident flow ($-v_{sh} > 0$) can only occur for a sufficiently high density jump, namely $n_1/n_0 > M_{in}^2$; consequently for M_{in} =1.05, 1.1, 1.2, and 1.3 this means that shocks should not be able to leave the laser beam cross-section and propagate freely unless n_1/n_0 >1.10, 1.21, 1.44, and 1.69, respectively. The latter explains the fact that the data curves for M_{in} =1.3 shown in Fig. 6 are partially incomplete for smaller $\langle U\rangle/T$ values, and that the corresponding data points (black) for M =1.3 and $\langle U\rangle/T_e$ <0.08 have been deduces with large uncertainties from the simulations. On the other hand, as Fig. 6 illustrates, the strength of the shock in terms of the jump conditions increases with M_{in}, as a consequence of the criterion $n_1/n_0 > M_{in}^2$, and increases with the cumulative action of the ponderomotive force in the beam speckles, $\propto \langle U\rangle/T_e$.

The time to observe the freely propagating shock separated from the laser beam cross-section can be very long, sometimes beyond the run time of our simulations. This is subject of a further discussion in the concluding section.

The speed of the emerging shock depends on the ponderomotive force exerted cumulatively by different speckles. Its value, as a function of the average ponderomotive potential $\langle U\rangle$ can be determined by integrating Eq. (19) from the upstream region of unperturbed plasma over the shock front into the region of the speckle pattern. For the cases of RPP, without temporal smoothing (i.e. not for SSD), the following relation between both sides of the shock results,

$$\frac{u_0^2}{c_s^2} = \frac{u_1^2}{c_s^2} + \ln\left(\frac{n_1}{n_0}\right)^2 + 2\frac{\langle U\rangle}{T_e} \qquad (23)$$

which yields a relation between $M_0 = u_0/c_S$, the density ratio n_1/n_0 and $\langle U\rangle/T_e$. With the continuity in the shock frame,

one obtains

$$M_0^2 = \frac{\ln(n_1/n_0)^2 + 2\langle U\rangle/T_e}{1-(n_1/n_0)^{-2}}. \quad (24)$$

The evaluation of expression Eq. (24) using numerical results from our hydrodynamic simulations is compared to the directly determined values of $-v_{\rm sh}/c_s = M_0 - M_{in}$ and shown in Fig. 7. The jump in the density n_1/n_0 corresponding to the shock, necessary to compute Eq. (24) together with the value of $\langle U\rangle/T_e$, are taken from the simulation results summarized in Fig. 6.

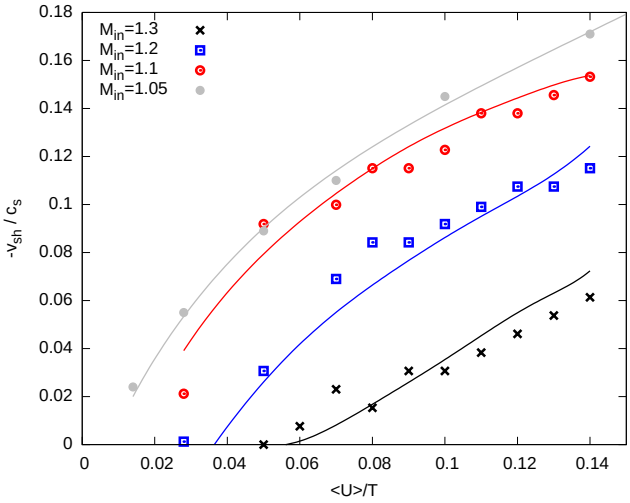

FIG. 7. Shock speed $v_{\rm sh}$ (in the laboratory frame) related to the sound speed c_s, as a function of the ponderomotive potential, deduced from hydrodynamic simulations with supersonic flow under the influence of a laser beam smoothed with RPP, for M_{in} =1.05 (marker in gray), 1.1 (red) 1.2 (blue), and 1.3 (black). Curves in the respective colors show the shock speed values expected from Eq. (24) depending on the average ponderomotive potential $\langle U\rangle/T_e$ and on the density ratio, n_1/n_0, for which the values shown in Fig. 6 have been used.

Inspecting Fig. 7 it becomes evident that for values of $\langle U\rangle/T_e$ <0.04 it is difficult to observe a shock outbreak in simulations, i.e. the freely propagating shock that is separated from the laser. The data shown as '○' symbols in Fig. 7 have therefore particularly low reliability for $\langle U\rangle/T_e$ <0.08.

In general, the time to observe the shock outbreak increases considerably with M_{in}. This is a consequence of the decrease of the drag with increasing M_{in} as $1/M_{in}^2$ as shown in Eq. (15). For M_{in} =1.3 shock outbreak is only observed for higher values $\langle U\rangle/T_e$ >0.05. It is also consistent with the criterion that for $-v_{sh}/c_s$ >0 the density jump in the shock has to be strong enough. This criterion relates n_1/n_0 to M_{in} via $-v_{sh}/c_s = M_0 - M_{in}$, which is for the case of an isothermal plasma $n_1/n_0 > M_{in}^2$, and follows from Eq. (A.4) for the general case for any γ value.

An approximate criterion for possible shock outbreak can be obtained by combining Eqs. (A.8) and (24) which yields $(\langle U\rangle/T_e) > \frac{1}{2}\left(M_{in}^2 - M_{in}^{-2} - 2\ln M_{in}^2\right) \simeq \frac{4}{3}(M_{in}-1)^3$ for weakly supersonic flow. The resulting $\langle U\rangle/T_e$ values above which shock outbreak can be expected for M_{in} =1.1, 1.2, and 1.3 are, respectively, $(\langle U\rangle/T_e) > 0.001$, 0.008, and 0.024. They are below the values for which we observe shock outbreak in our simulations, e.g. for M_{in} =1.3 we observe twice as large the magnitude of $\langle U\rangle/T_e$. Note that we have used here the criterion that does not account for the gradual transition of $\langle U\rangle/T_e$ as a function of y in the simulations.

C. Beams with temporal smoothing

In the preceding sections the formation of a ponderomotively driven bow shock was considered for the case of an optically smoothed laser beam with merely spatial incoherence due to the introduction of a random phase plate in the near field. Modern laser facilities also include spatio-temporal smoothing techniques. Smoothing by Spectral Dispersion (SSD) is implemented on all the major ICF and high-energy density laser facilities such as the NIF, Omega and LMJ lasers[28–30].

The effect of SSD on beam deflection and consequently on the bow shock formation is modified by the non stationary features of the beam speckle pattern.[12,22,31] SSD is a method

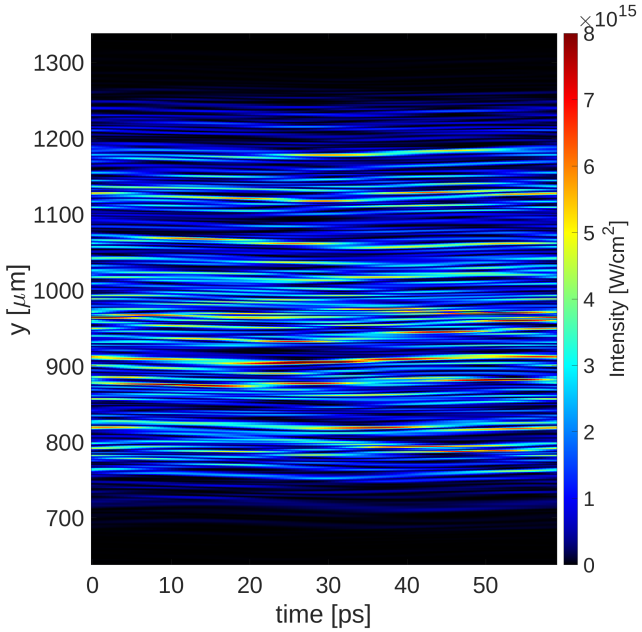

FIG. 8. A line-out of the laser intensity profile at best focus is displayed as a function of time showing sinusoidal motion of the laser speckles along the direction of spectral dispersion (y-direction). The profile along the x-direction also contains speckles but the speckles do not move in the x-direction. The SSD modulation frequency of 17GHz has a repeat period of 58.8ps, simulations ran for several nanoseconds (>30 SSD periods).

of using bandwidth in combination with a grating to produce speckle movement. This method was originally proposed[32] for temporally smoothing laser focal spots.

In this article we focus on 1D transverse SSD as is implemented on the NIF. The first stage of SSD is to apply a sinusoidal phase modulation to the pulse, which introduces bandwidth. The beam then passes through a dispersion grat-

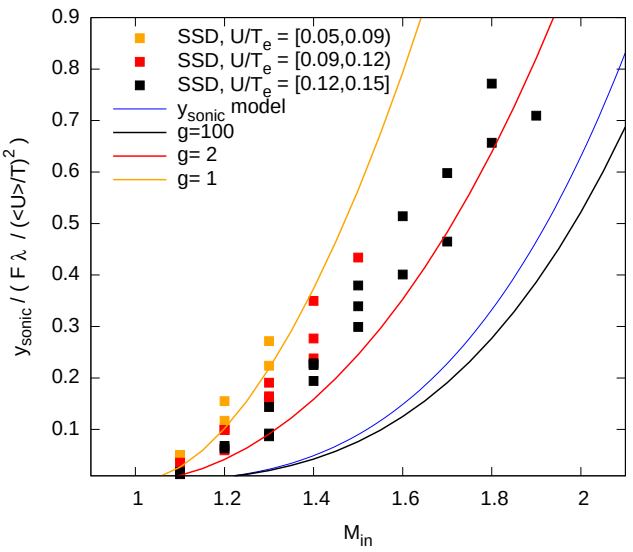

FIG. 9. Similar to Fig. 2, position of the sonic flow as a function of the incoming flow Mach number M_{in} from hydrodynamic simulations with laser beams smoothed with the SSD method, parameters: n/n_c =0.1, $F = 8$, SSD bandwidth 17 GHz and δ_m =0.6. The colour of the data points indicates the range of the average ponderomotive potential, orange for $0.05 \leq \langle U\rangle/T_e < 0.09$, red for $0.09 \leq \langle U\rangle/T_e < 0.12$, and black for $0.12 \leq \langle U\rangle/T_e < 0.15$. The y_{sonic} values corresponding to the model Eqs. (27-28) are shown as coloured curves for the parameter values g =1, 2, and 100. The curve labelled 'y_{sonic} model' corresponds to the Eq. (22) as also shown in Fig. 2.

ing which tilts the pulse front and results in a distribution of frequencies across the lens, typically along one dimension. The resulting electric field at the lens can be expressed as:

$$\mathbf{E}(y,t) = \frac{1}{2}\mathbf{E}_0(y,t)e^{i[\omega_0 t+\delta_m \sin(\omega_m t+\alpha y)+\phi_0]} + c.c., \qquad (25)$$

where ω_0 is the central angular frequency of the laser, ϕ_0 is the initial phase, ω_m is the modulation frequency, and δ_m is the modulation depth. Here $\alpha = 2\pi N_{cc}/w_y$, where N_{cc} is the number of color cycles and w_y is the width of the beam along the y-direction at the lens. The total bandwidth added to the laser is $\Delta\omega \approx 2\delta_m\omega_m$ which is small relative to the laser frequency $\Delta\omega \ll \omega_0$. The effect of SSD at a laser's best focus for our simulation parameters is demonstrated in Fig. 8, which shows sinusoidal motion of the laser speckles in time, along the direction of angular dispersion.

D. Analytical model of beam bending and shock onset with spatio-temporal smoothing

The characteristic distance y_{sonic}, Eq. (22), can be obtained from the solution of Eq. (20) with the suitable expression for the drag coefficient α, Eq. (18), and the beam deflection rate Eq. (10). For an approximate choice of electric field temporal correlation function, the calculation of beam deflection has been reduced in Ref. 12 to evaluation of a two-dimensional integral in the Fourier space. The analytical theory of beam deflection by a flow in Ref. 12 has been derived for the case of a laser beam which is spatially smoothed by an RPP and temporally smoothed by the random phase modulations, similar to SSD Eq. (25), that was used for analytical analysis. Following results of Ref. 12 in the limit of large bandwidth and finite Landau damping, Eq. (45) in Ref. 12, we have for the drag coefficient

$$\alpha = \left(\frac{\langle U\rangle}{T_e}\right)^2 \frac{k_0 c_s}{FM}\,\Xi(M,\nu_{ia},g,N_{cc}), \qquad (26)$$

where the two-dimensional integral reads

$$\Xi(M,\nu_{ia},g,N_{cc}) = i\int d\phi \int d\kappa\kappa^2 \frac{\hat{c}(\kappa)\,\cos\phi}{1-u^2-i\,2\nu_{ia}u}. \qquad (27)$$

In the one-dimensional realization of the SSD where the speckles move along the direction y of the background plasma flow the argument u of the integral is given by

$$u = \frac{i}{g\kappa}\left(1-e^{-N_{cc}\kappa\cos\phi}\right) - \frac{\kappa M\cos\phi}{\kappa}, \qquad (28)$$

where $g = k_0 c_s/(F\gamma)$ can be understood as the ratio between the correlation time of the electric field correlation, $1/\gamma$, and the ion acoustic transit time over the width of a speckle, $F/(k_0 c_s)$. The function $\hat{c}(\kappa)$ is given by Eq.(32) from Ref. 12. In the large bandwidth limit $N_{cc}\gamma/\omega_m \gg 1$. We have used Eq. (26) for the drag coefficient α to obtain y_{sonic} from Eq. (20) and results are plotted in Fig. 9 for $g = 1, 2$, i.e. for short field correlation times, and $g = 100$ which is very close to the RPP result, Eq.(22).

E. Shock formation by SSD beams

Consequently we have also carried out simulations by using laser beams generated with RPP and SSD for the case of SSD, in complement to our study for beams with RPP only. For this study we have used the color cycle $N_{cc} = 1$, the depth δ_m = 0.6, and the modulation frequency $\omega_m = 2\pi \times 17GHz$, similar to the NIF laser at the National Ignition Facility. We generated 128 snapshots of the laser focal spot during one SSD period $\tau_{SSD} = 2\pi/\omega_m \approx 58.8ps$ so that for each hydro time step the next snapshot was used and the snapshots repeated. Results of this method are consistent with speckle velocity theory[33]. At the laser focus the speckles have sinusoidal motion along the direction of SSD (y-direction) in time as shown in figure 8.

In reminiscence to the results for RPP beams shown in Figs. 2 and 5, we have plotted the scaled values of y_{sonic} for the simulations of SSD cases in Fig. 9 and for the density jumps n_1/n_0 comparing the RPP simulations (solid lines) with SSD simulations (dashed).

The action of spatio-temporal smoothing has influence on the position in the plasma, y_{sonic}, at which the plasma flow is slowed down to $M = 1$. While this position proves to be shifted further inside the speckle pattern with respect to the case of only spatial smoothing with RPP, see Fig. 2, the shock density jump for the cases with SSD may be stronger than for

the corresponding RPP cases, see Fig. 5, at least for quite pronounced ponderomotive drive with $\langle U\rangle/T_e > 0.1$. The latter may be attributed to the fact that the speckle motion in y-direction, inherent to SSD with modulation in and against the direction of the incoming flow, occupies a greater spatial region around the speckle center and so can potentially expel a greater "mass" by the ponderomotive action, reinforcing the shock strength.

V. CONCLUSIONS AND IMPLICATIONS FOR ICF EXPERIMENTS

Speckled laser beam propagation in plasma slab or cylindrical geometries with perpendicular supersonic plasma inflow and laser-plasma coupling through the ponderomotive force always leads to a macroscopic shock formation provided the plasma can propagate into a thick enough laser beam. The characteristic distance of plasma penetration across the randomized laser beam required for the flow to slow down to subsonic velocity and form a shock is given by Eq. (22). This analytical result was derived in the slab geometry and confirmed in numerical simulations where the laser beam of a cylindrical cross-section had a large diameter giving rise to a bow shock. The physics of the shock formation is related to the beam bending processes due to the plasma flow and the plasma reaction to the momentum change induced by the redirected laser light.

We have performed numerical simulations for laser coupling to the plasma hydrodynamics over the laser beam cross section which clearly show the shock formation. In one of the numerical examples based on the RPP beam results of Sec. III and Fig. 2 we take for the beam intensity $I = 2\times10^{15}$ W/cm^2 and electron temperature T_e=2 keV obtaining the average, normalized ponderomotive potential $\langle U\rangle/T_e \approx 0.011$. With $F\lambda$=1μm and e.g. an incoming flow velocity corresponding to $1.05 \leq M_{in} \leq 1.2$, the distance y_{sonic} to shock formation within the laser is approximately 0.05-0.1 $F\lambda/(\langle U\rangle/T_e)^2$ (see Figs. 2 and 9), i.e. approximately 400-810μm. To estimate a time necessary to generate the shock we take this distance and divide it by the sound speed obtaining roughly 1.3-2.7 ns. Thus within the square of 400μm$\times$ 400μm or 810μm $\times$ 810μm a laser beam of average intensity $I = 2\times10^{15}$ W/cm^2 will require 9kJ or 36kJ, respectively, as energy. These are energy requirements that can be realized at the NIF, but may require specially crafted conditions in order to observe a shock in experiments.

The theory describing the deceleration of plasma flow to subsonic speeds, thereby promoting shock generation, has been derived specifically for isothermal plasmas. This formulation is based on beam bending calculations for laser beams that are spatially and temporally smoothed. Consistently, nonlinear shock modeling using hydrodynamic simulations has been conducted, considering the effects of ponderomotive laser-plasma coupling, while disregarding factors such as laser absorption and plasma heating. We expect that during experiments employing less energetic lasers, as demonstrated in the context of the OMEGA facility[15], thermal effects[20,34,35] will assume a more pronounced role. Consequently, this is expected to lower the threshold for shock generation and amplify its strength.

ACKNOWLEDGMENTS

Simulations carried out by SH were granted access to the French HPC resources of IDRIS under the allocations A0100500573 and AD010500573R1 by GENCI, France. SH acknowledges the support by the CPHT computer team. We acknowledge support from the Digital Research Alliance of Canada.

This work was performed under the auspices of the U.S. Department of Energy by Lawrence Livermore National Laboratory under Contract DE-AC52-07NA27344 and by LLNL's WPD, ICF Program's Academic Collaboration Teams's University Program (ACT-UP) under Subcontract No. B645970.

REFERENCES

[1] W. L. Kruer, S. C. Wilks, B. B. Afeyan, and R. K. Kirkwood, Phys. Plasmas **3**, 382 (1996).
[2] R. K. Kirkwood, B. B. Afeyan, W. L. Kruer, B. J. MacGowan, J. D. Moody, D. S. Montgomery, D. M. Pennington, T. L. Weiland, and S. C. Wilks, Phys. Rev. Lett. **76**, 2065 (1996).
[3] V. V. Eliseev, W. Rozmus, V. T. Tikhonchuk, and C. E. Capjack, Physics of Plasmas **3**, 2215 (1996).
[4] P. Michel, L. Divol, E. A. Williams, S. Weber, C. A. Thomas, D. A. Callahan, S. W. Haan, J. D. Salmonson, S. Dixit, D. E. Hinkel, M. J. Edwards, B. J. MacGowan, J. D. Lindl, S. H. Glenzer, and L. J. Suter, Phys. Rev. Lett. **102**, 025004 (2009).
[5] P. Michel, L. Divol, E. A. Williams, C. A. Thomas, D. A. Callahan, S. Weber, S. W. Haan, J. D. Salmonson, N. B. Meezan, O. L. Landen, S. Dixit, D. E. Hinkel, M. J. Edwards, B. J. MacGowan, J. D. Lindl, S. H. Glenzer, and L. J. Suter, Phys. Plasmas **16**, 042702 (2009).
[6] P. Michel, S. H. Glenzer, L. Divol, D. K. Bradley, D. Callahan, S. Dixit, S. Glenn, D. Hinkel, R. K. Kirkwood, J. L. Kline, W. L. Kruer, G. A. Kyrala, S. Le Pape, N. B. Meezan, R. Town, K. Widmann, E. A. Williams, B. J. MacGowan, J. Lindl, and L. J. Suter, Phys. Plasmas **17**, 056305 (2010).
[7] A. Colaïtis, S. Hüller, D. Pesme, G. Duchateau, and V. T. Tikhonchuk, Physics of Plasmas **23**, 032118 (2016).
[8] D. E. Hinkel, E. A. Williams, and C. H. Still, Phys. Rev. Lett. **77**, 1298 (1996).
[9] H. A. Rose, Physics of Plasmas **3**, 1709 (1996).
[10] J. D. Moody, B. J. MacGowan, D. E. Hinkel, W. L. Kruer, E. A. Williams, K. Estabrook, R. L. Berger, R. K. Kirkwood, D. S. Montgomery, and T. D. Shepard, Phys. Rev. Lett. **77**, 1294 (1996).
[11] B. Bezzerides, Physics of Plasmas **5**, 2712 (1998).
[12] H. A. Rose and S. Ghosal, Physics of Plasmas **5**, 775 (1998).
[13] S. Ghosal and H. A. Rose, Physics of Plasmas **4**, 2376 (1997).
[14] S. Ghosal and H. A. Rose, Physics of Plasmas **4**, 4189 (1997).
[15] A. L. Milder, et al., in preparation for Phys. Plasmas.
[16] J. Candy, W. Rozmus, and V. T. Tikhonchuk, Phys. Rev. Lett. **65**, 1889 (1990).
[17] S. Hüller, Physics of Fluids B: Plasma Physics **3**, 3317 (1991).
[18] H. A. Rose, Physics of Plasmas **4**, 437 (1997).
[19] R. W. Short, R. Bingham, and E. A. Williams, Phys. Fluids **25**, 2302 (1982).
[20] A. J. Schmitt, Physics of Fluids B **1**, 1287 (1989).
[21] D. E. Hinkel, E. A. Williams, and C. H. Still, Phys. Rev. Lett. **77**, 1298 (1996).
[22] C. Ruyer, P. Loiseau, G. Riazuelo, R. Riquier, A. Debayle, P. E. Masson-Laborde, and O. Morice, Matter and Radiation at Extremes **8**, 025901 (2023).
[23] S. Ghosal and H. A. Rose, Physics of Plasmas **4**, 4189 (1997).

[24] R. J. LeVeque, *Numerical methods for conservation laws (2. ed.).*, Lectures in mathematics (Birkhäuser, 1992) pp. 1–214.
[25] S. Hüller, P. E. Masson-Laborde, D. Pesme, M. Casanova, F. Detering, and A. Maximov, Phys. Plasmas **13**, 022703 (2006).
[26] R. J. L. Vecque, J. Comp. Phys. **131**, 327?353 (1997).
[27] By separation of variables in Eq. (21), an integral $\int_{y=0}^{y_{sonic}}(U(y)/T)^2 dy$ is applied, with $U(y)$ denoting the local value of the envelope of the ponderomotive potential, with $U(y=0)=0$ and $U(y)\longrightarrow\langle U\rangle$ for y inside the beam. This yields a correction to Eq. (22).
[28] T. R. Boehly, V. N. Goncharov, O. Gotchev, J. P. Knauer, D. D. Meyerhofer, D. Oron, S. P. Regan, Y. Srebro, W. Seka, D. Shvarts, S. Skupsky, and V. A. Smalyuk, Physics of Plasmas **8**, 2331 (2001).
[29] D. H. Kalantar, M. H. Key, L. B. DaSilva., S. G. Glendinning, J. P. Knauer, B. A. Remington, F. Weber, and S. V. Weber, Phys. Rev. Lett. **76**, 3574 (1996).
[30] V. N. Goncharov, S. Skupsky, T. R. Boehly, J. P. Knauer, P. McKenty, V. A. Smalyuk, R. P. J. Town, O. V. Gotchev, R. Betti, and D. D. Meyerhofer, Physics of Plasmas **7**, 2062 (2000).
[31] S. Hüller, G. Raj, M. Luo, W. Rozmus, and D. Pesme, Phil. Trans. Royal Society A **378**, 20200038 (2020), DOI:10.1098/rsta.2020.0038.
[32] S. Skupsky, R. W. Short, T. Kessler, R. S. Craxton, S. Letzring, and J. M. Soures, Journal of Applied Physics **66**, 3456 (1989), https://doi.org/10.1063/1.344101.
[33] F. Walraet, G. Bonnaud, and G. Riazuelo, Physics of Plasmas **8**, 4717 (2001).
[34] R. L. Berger, B. F. Lasinski, A. B. Langdon, T. B. Kaiser, B. B. Afeyan, B. I. Cohen, C. H. Still, and E. A. Williams, Phys. Rev. Lett. **75**, 1078 (1995).
[35] L. Yin, K. L. Nguyen, B. J. Albright, A. G. Seaton, A. M. Hansen, D. H. Froula, D. Turnbull, and J. P. Palastro, Physics of Plasmas **30**, 102703 (2023).
[36] J. Spurk and N. Aksel, *Fluid Mechanics* (Springer International Publishing, 2019) Chap. 9.2.3.
[37] P. Mulser, "Hot matter from high-power lasers," (Springer International Publishing, 2020) pp. 236–255.

Appendix: Rankine-Hugoniot shock relations

The Rankine-Hugoniot relations between the zones '0' for the unperturbed plasma and '1' for the zone behind the shock, propagating with v_{sh}, readily read[36,37]

$$n_0(v_{y,0}-v_{sh}) = n_0M_0c_{s,0} = n_1M_1c_{s,1} = n_1(v_{y,1}-v_{sh}) \quad \text{(A.1)}$$

$$n_0M_0^2c_{s,0}^2 + p_0 = n_1M_1^2c_{s,1} + p_1 \ , \text{ and} \quad \text{(A.2)}$$

$$h_0 + M_0^2c_{s,0}^2/2 = h_1 + M_1^2c_{s,1}^2/2, \quad \text{(A.3)}$$

with $p_{1,2}$ denoting here the pressures, $h_{0,1} = p_{0,1}/n_{0,1} + \varepsilon_{0,1}$ the enthalpies, and $\varepsilon_{0,1}$ the internal energies . These relations express the balance for the continuity, the momentum (Euler equation), and the energy (Bernoulli equation) between each side, respectively, supposing steady state and absence of any potential force on either side.

The shock discontinuity in general includes ion heating with entropy increase over the shock front[37], yielding a jump in density and in temperature,

$$n_1/n_0 = \tfrac{\gamma+1}{2}M_0^2/[1+\tfrac{\gamma-1}{2}M_0^2] \ , \quad \text{(A.4)}$$

$$T_1/T_0 = (2\gamma M_0^2 + 1 - \gamma)/[(\gamma-1)(n_1/n_0)] \ . \quad \text{(A.5)}$$

The case of an isothermal plasma (with $\gamma = 1$, degrees of freedom $\to\infty$) is a particular case, for which Eq. (A.3), relating the internal energies on both sides, can be disregarded.

$\langle U\rangle/T$	M_{in}	n_1/n_0	n_0M_0	n_1M_1	π_0	π_1	type
0.073	1.1	1.39	1.26	1.27	2.58	2.56	RPP
0.10	1.1	1.51	1.29	1.33	2.66	2.68	RPP
0.11	1.1	1.54	1.29	1.32	2.67	2.66	RPP
0.1	1.2	1.64	1.33	1.39	2.77	2.81	RPP
0.11	1.2	1.67	1.35	1.40	2.82	2.83	RPP
0.13	1.2	1.74	1.36	1.38	2.86	2.85	RPP
0.073	1.1	1.31	1.18	1.20	2.40	2.42	SSD δ_m =0.6
0.143	1.1	1.86	1.46	1.54	3.15	3.14	SSD δ_m =0.6
M_{in}	$\langle U\rangle/T$	n_1/n_0	n_0M_0	n_1M_1	π_0	π_1	type
1.1	0.10	1.51	1.29	1.27	2.58	2.56	RPP
1.2	0.10	1.64	1.33	1.39	2.77	2.81	RPP
1.3	0.10	1.71	1.40	1.37	2.95	2.80	RPP
1.1	0.143	1.86	1.46	1.54	3.15	3.14	SSD δ_m =0.6
1.2	0.143	2.06	1.52	1.59	3.31	3.30	SSD δ_m =0.6

TABLE I.

We consider here the isothermal plasma case for simplicity, also in the simulations, with $c_{s,0} = c_{s,1} \equiv c_s$, by disregarding Eq. (A.3), so that the system of relations reduces to

$$n_0M_0 = n_1M_1, \quad \text{(A.6)}$$

$$\pi_0 := n_0(M_0^2+1) = n_1(M_1^2+1) =: \pi_1 \ . \quad \text{(A.7)}$$

The resulting density jump is then essentially a function of the Mach numbers, $n_1/n_0 = M_0^2 = M_1^{-2}$ with $M_0M_1 = 1$.

From the simulations one can determine the shock speed in the laboratory frame, v_{sh}, which can be deduced from the space-time slope of the shock front as seen in Figs. 4. One can consequently determine the Mach numbers M_0 and M_1 on each side of the shock, furthermore n_1, while n_0 and M_{in} are known from the unperturbed plasma. Knowing these value, the values for $M_0 = M_{in} - v_{sh}/c_s$, for $M_1 = (v_{y,1} - v_{sh})/c_s$, and the ratio n_1/n_0 can be deduced. It furthermore follows

$$-v_{sh}/c_s = \sqrt{n_1/n_0} - M_{in} \ , \quad \text{(A.8)}$$

which has the consequence that the outbreak of a shock running against the incident flow, namely $-v_{sh} > 0$, can only occur for a sufficiently high density jump, namely $n_1/n_0 > M_{in}^2$. Table I shows the results for simulations of selected RPP and SSD cases. The balance between the Rankine-Hugoniot relations conserving mass- and momentum flow on each side of the shock, in the proper frame of the shock, is generally quite well reproduced, as expected for well-developed shocks. One can find a generally better balance for the momentum flow, $\pi_j = n_j(M_j^2+1)$, j=0,1. The discrepancy in the mass balance n_jM_j slightly increases, however, systematically with $\langle U\rangle/T$.